Paschen-Back effects and Rydberg-state diamagnetism in vapor-cell electromagnetically induced transparency

L. Ma,[1] D. A. Anderson,[2] and G. Raithel[1,2]

[1]*Department of Physics, University of Michigan, Ann Arbor, Michigan 48109, USA*
[2]*Rydberg Technologies LLC, Ann Arbor, Michigan 48104, USA*

We report on rubidium vapor-cell Rydberg electromagnetically induced transparency (EIT) in a 0.7 T magnetic field where all involved levels are in the hyperfine Paschen-Back regime, and the Rydberg state exhibits a strong diamagnetic interaction. Signals from both ^{85}Rb and ^{87}Rb are present in the EIT spectra. Isotope-mixed Rb cells allow us to measure the field strength to within a $\pm 0.12\%$ relative uncertainty. The measured spectra are in excellent agreement with the results of a Monte Carlo calculation and indicate unexpectedly large Rydberg-level dephasing rates. Line shifts and broadenings due to magnetic-field inhomogeneities are included in the model.

I. INTRODUCTION

Electromagnetically induced transparency (EIT) is a quantum interference process in which two excitation pathways in a three-level atomic system destructively interfere and produce an increase in the transmission of the probe laser beam [1,2]. In the Rydberg-EIT cascade scheme [3], the transparency is formed by a coherent superposition of the ground and Rydberg states. Rydberg-EIT has been implemented in both cold atomic gases [4,5] and in room-temperature vapor cells [3,6]. It has been widely used as a nondestructive optical detection technique for Rydberg spectra [7,8], quantum information processing [9], and measurements of weak [10,11] and strong [12,13] microwave electric fields. EIT in vapor cells has been employed to investigate Cs Rydberg atoms in magnetic fields up to $\sim$0.01 T [14] and Rb $5D_{5/2}$ atoms in fields up to $\sim$0.6 T [15,16].

Here, we investigate Rydberg atoms in a 0.7 T magnetic field. In magnetic fields $B > 2n^{-4}$ a.u. (0.4 T for principal quantum number $n = 33$), the diamagnetic term dominates and mixes states with different angular momentum [17]. We employ the $|33S_{1/2}, m_j = 1/2\rangle$ Rydberg state whose interaction with the B field includes a Zeeman (linear) and a diamagnetic (quadratic) term. In a 0.7 Tesla field, the diamagnetic interaction accounts for about 70% of the differential magnetic dipole moment $-dE_r/dB = 3.06\mu_B$ (E_r is the Rydberg-state energy, μ_B is the Bohr magneton). In this field, all involved states are in the hyperfine Paschen-Back regime, and the energy separations between the magnetic states are larger than the Doppler width in room-temperature spectroscopic cells.

The presented method offers two advantages in high-magnetic-field measurements. First, the diamagnetic interaction gives rise to an enhanced differential dipole moment, enabling measurement of small changes of a large magnetic field. Second, simultaneous measurement of field-induced level shifts for both ^{85}Rb and ^{87}Rb isotopes affords high absolute accuracy in magnetic field measurements based on relative line separations.

II. EXPERIMENTAL SETUP

The magnetic field is produced by two N52 Neodymium permanent magnets. The B field is calculated using a finite-element analysis software (ANSYS Maxwell). Figures 1(a) and 1(b) show cuts of the magnetic field. A spectroscopic cell filled with a natural Rb isotope mix is placed between the magnets. In order to increase the optical absorption, the cell temperature is maintained at $\sim$45 °C by heating both the cell and surrounding magnets.

The optical setup includes two measurement channels: a Rydberg-EIT and a saturation spectroscopy (Sat. Spec.) channel. As shown in Figs. 1(b) and 1(c), the channels are parallel to the x axis and separated by 1.85 mm in the y direction. The Rydberg-EIT probe beam is focused to a waist of $\sim$40 μm ($1/e^2$ radius) and has a power of $\sim$1 μW. The coupling beam has a waist of $\sim$100 μm and a power of $\sim$35 mW. The polarizations of the coupling and probe beams are both linear and parallel to the magnetic field along z. The probe laser frequency is common to both channels and is frequency modulated by the same acousto-optic modulator. The probe modulation results in a minor broadening of the EIT lines that, in future implementations, can be avoided by only modulating the Sat. Spec. probe beam. The demodulated Sat. Spec. signals are used to lock the probe laser beam to a $5S_{1/2}$ to $5P_{3/2}$ transition (most are shown in Fig. 2(a)).

The Rydberg-EIT coupling laser is linearly scanned over a range of 4.5 GHz at a repetition rate of $\sim$1 Hz. The scans are linearized to within a 1 MHz residual uncertainty using the transmission peaks of a temperature-stabilized Fabry-Perot cavity. The coupler laser is chopped at 33 kHz. The EIT transmission signals are recovered by a digital lock-in referenced to the chopping frequency.

III. RYDBERG-EIT SPECTRA IN THE HIGH-MAGNETIC-FIELD REGIME

At $B \sim 1$ T, the energy levels are shifted by up to several tens of GHz. The relevant ground- ($5S_{1/2}$) and intermediate-state ($5P_{3/2}$) energy levels and calculations of their field-induced shifts are plotted in Figs. 2(b) and 2(c). In order to frequency stabilize the EIT probe laser to a $5S_{1/2}$–$5P_{3/2}$ transition, we implement a Sat. Spec. channel in the high-B region, as illustrated in Fig. 1. The right panel of Fig. 2(a) shows the measured saturated absorption signals. Over the displayed probe frequency range, the spectrum consists of four
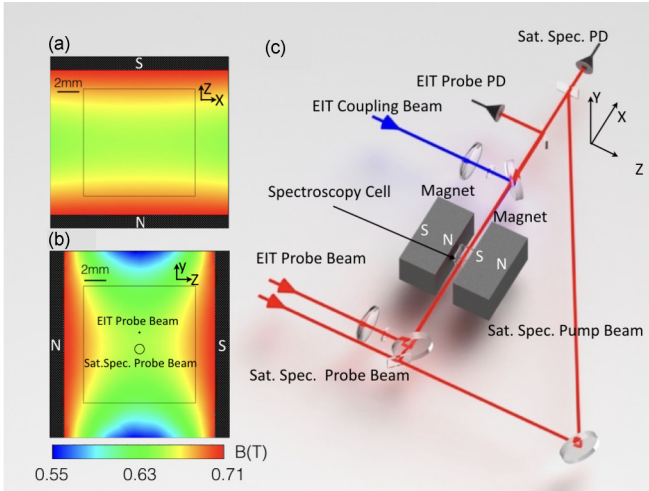
FIG. 1. Calculation of the magnetic field B in the (a) x-z plane and (b) y-z plane. The filled black regions represent the poles of the bar magnets. The open black square represents the inner boundary of the spectroscopy cell. (c) Illustration of the experimental setup, including an EIT channel and a saturation spectroscopy channel. The two channels are separated in the y direction.
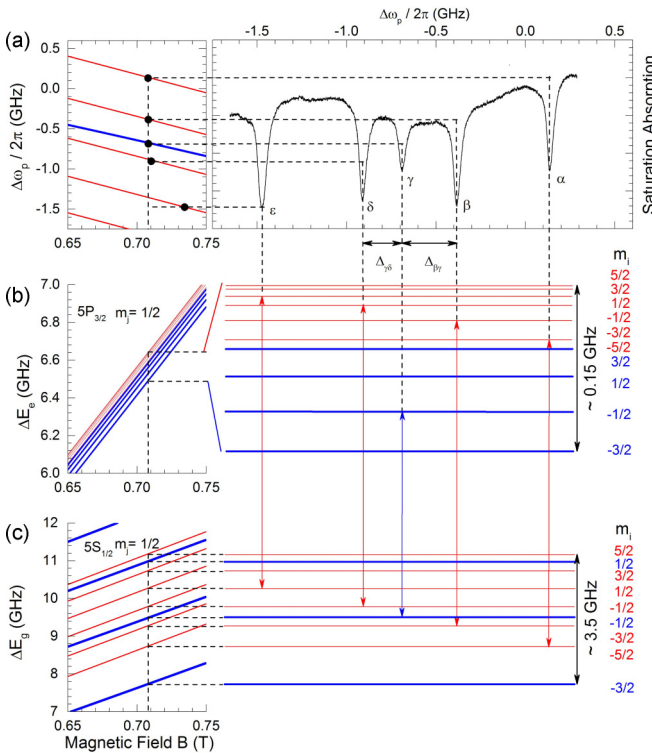

FIG. 2. (a) Saturation absorption signal in a 0.71 T magnetic field versus probe frequency detuning $\Delta\omega_p$ (right) and calculated magnetic-field-induced level shifts (left). The frequency is measured relative to the magnetic-field-free ^{87}Rb $5S_{1/2}, F = 2$ to $5P_{3/2}, F = 3$ transition, where $\Delta\omega_p = 0$. The linewidth is dominated by inhomogeneous broadening due to the magnetic-field inhomogeneity. (b) Schematic of atomic energy levels for intermediate state and (c) ground state. The states are labeled by the quantum numbers m_i and m_j (which are good quantum numbers in the Paschen-Back regime). Energy levels of ^{85}Rb and ^{87}Rb are shown in thin red and bold blue, respectively.

^{87}Rb lines (peaks α, β, δ, and ϵ) and a ^{85}Rb line (peak γ). In the Paschen-Back limit, crossover dips are not present because the m_i quantum number is conserved in all optical transitions ($\Delta m_i = 0$), and because for π-polarized light the selection rule $\Delta m_j = 0$ applies. Also, the separations between the fine structure transitions with different m_j exceed the Doppler width; here, we are selecting the $m_j = 1/2$ levels.

Due to the differences in the hyperfine coupling of ^{87}Rb and ^{85}Rb (magnetic dipole coupling strength, electric quadrupole coupling strength, nuclear spins, and isotope shifts), the energy levels of each isotope exhibit differential shifts. In our calculation, we follow Ref. [18] and references therein. The gap ratio $\Delta_{\gamma\delta}/\Delta_{\beta\gamma}$ is found to be sensitive to the magnetic field. Using this feature, which relies on the presence of both isotopes in the cell, we determined the magnetic field strength in the Sat. Spec. channel to be 0.71 T. This is indicated by the vertical dashed line in the left panel of Fig. 2(a). At the end of the scan range, the peak positions deviate slightly from their locations expected for 0.71 T. This is caused by a slight nonlinearity of the mechanical-grating scan of the external-cavity diode laser. This nonlinearity does not affect the Rydberg-EIT experiment, discussed in the next paragraph, because there the probe laser is locked to a Sat. Spec. peak [five out of six are shown in Fig. 2(a)] and has a fixed frequency.

To investigate Rydberg-EIT in the high-B regime, we frequency-stabilize the π-polarized EIT probe laser to a $|5S_{1/2}, m_j = 1/2, m_i\rangle \rightarrow |5P_{3/2}, m_j = 1/2, m_i\rangle$ transition and access the $|33S_{1/2}, m_j = 1/2, m_i\rangle$ Rydberg state with a coupling laser of the same polarization. Figures 3(a)–3(f) show the Rydberg-EIT spectra measured at $B = 0.70$ T.

For Rydberg-EIT in a vapor cell, the atomic Maxwell velocity distribution needs to be considered, as well as the Doppler effect induced by the wavelength mismatches of the probe and coupler lasers [3]. If an external field shifts the ground, intermediate, and Rydberg levels by ΔE_g, ΔE_e, and ΔE_r, respectively, the coupling laser detunings, $\Delta\omega_c$, at which the EIT resonances occur are

$$\hbar\Delta\omega_c = \Delta E_r + \left(\frac{\lambda_p}{\lambda_c} - 1\right)\Delta E_e - \frac{\lambda_p}{\lambda_c}(\Delta E_g + \hbar\Delta\omega_p), \quad (1)$$

where λ_p and λ_c are the wavelengths of the probe and coupling lasers, and $\Delta\omega_p$ is the probe-laser detuning. The wavelength-dependent prefactors are deduced by requiring resonance on both the lower and the upper transitions in the three-level cascade structure.

The shifts ΔE_g, ΔE_e, and ΔE_r in Eq. (1) are plotted as a function of B in Figs. 3(g)–3(i). For S Rydberg states in Rb, which are nondegenerate and fine-structure-free, the Rydberg level shift (in atomic units) is [17]

$$\Delta E_r = \frac{g_s m_s B}{2} + \frac{B^2}{8}\langle nlm_l|\hat{r}^2\sin^2\hat\theta|nlm_l\rangle, \quad (2)$$

where l, m_l, and m_s are angular momentum, magnetic orbital and spin quantum numbers, respectively and $g_s \approx 2.00232$ is the electron g-factor. The coordinates r and θ are spherical coordinates of the Rydberg electron (**B** points along z). The first term on the right side of Eq. (2) represents the paramagnetic term of the electron spin, and the second term is the diamagnetic shift. For $|33S_{1/2}, m_j = 1/2\rangle$ atoms in a 1 T field, the differential dipole moment is 3.06 μ_B,
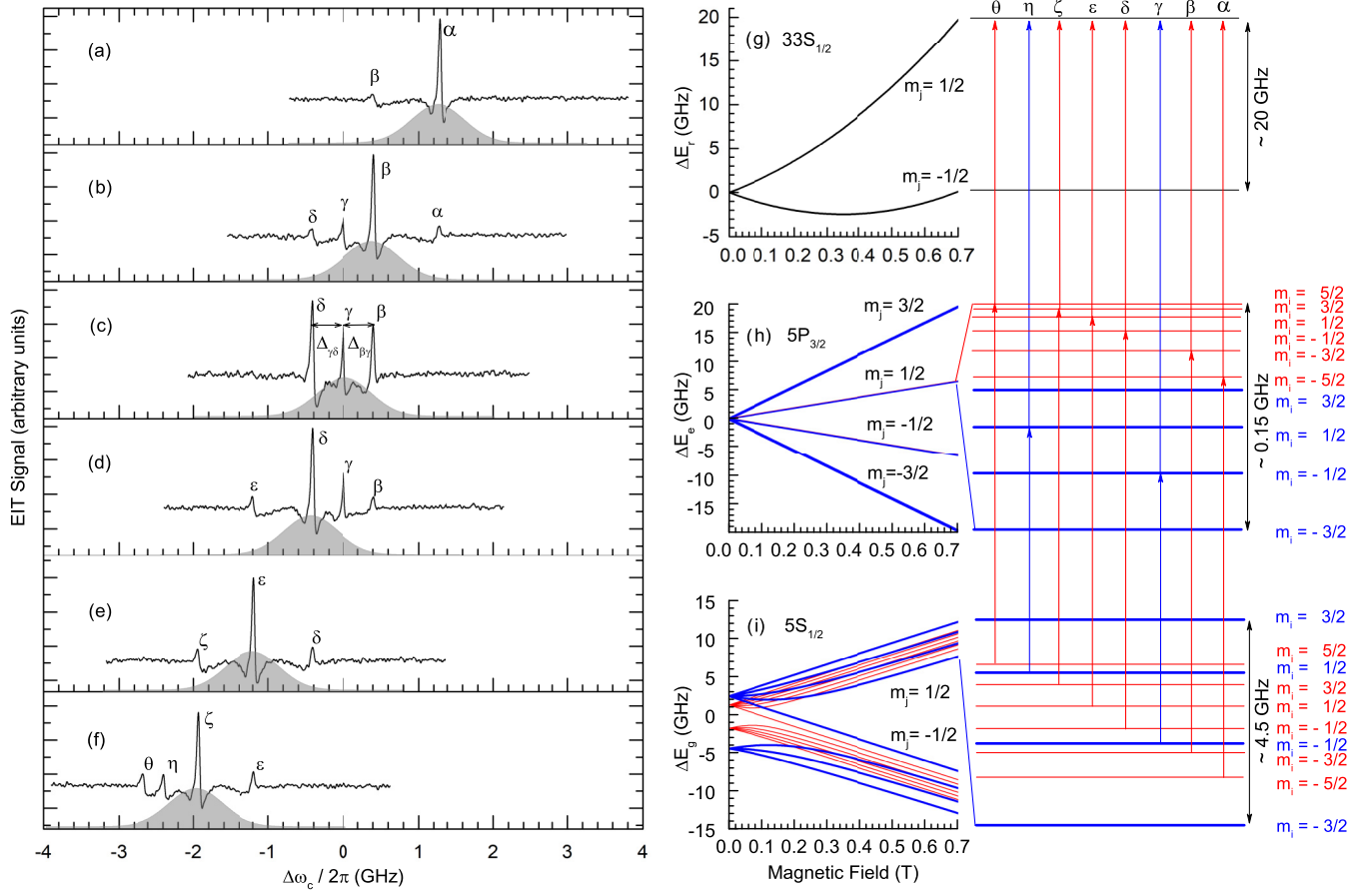
FIG. 3. (a)–(f) EIT transmission signals for the EIT probe laser locked to a Sat. Spec. peak. [The Sat. Spec. peaks α to ϵ are shown in Fig. 2(a).] The shaded areas indicate the weighting due to the Maxwell velocity distribution [see discussion of Eq. (3)]. Signals corresponding to the same EIT transition are labeled with the same Greek letter in the spectra. Same Greek letters are used to label the corresponding lower transition in Fig. 2. The coupling laser detuning is given relative to peak γ. The spectra are shifted such that shared EIT peaks are aligned, as determined using cross-correlation functions of neighboring scans. Calculated energy level shifts in the Paschen-Back regime for the (g) Rydberg, (h) intermediate, and (i) ground states. The transitions corresponding to the EIT resonances in (a)–(f) are indicated by vertical arrows and labeled with the same Greek letter. Transitions in ^{85}Rb and ^{87}Rb are coded with thin red and bold blue lines, respectively.

implying that the diamagnetic contribution is about twice as large as the spin dipole moment. This fact, as well as the λ_p/λ_c enhancement factor of the ground-state shift (ΔE_g), make the Rydberg-EIT resonances highly sensitive to small variations in a high-magnetic-field background (see Sec. IV).

Eight out of the ten EIT resonances that exist for the given polarization case are present in the frequency range covered by the coupling laser in Figs. 3(a)–3(f). Every resonance satisfies Eq. (1) and has a well-defined atomic velocity, v, given by

$$v = \frac{\lambda_p}{2\pi}\left(\Delta\omega_p + \frac{\Delta E_g - \Delta E_e}{\hbar}\right). \qquad (3)$$

For an EIT resonance to be visible in a spectrum with given $\Delta\omega_p$, ΔE_g, and ΔE_e, the velocity v that follows from Eq. (3) must be within the Maxwell velocity distribution. Since the probe laser is locked to one of the resonances shown in Fig. 2 in every EIT spectrum, each spectrum has a strong resonance at its center for which Eq. (3) yields $v \approx 0$ (where the Maxwell velocity distribution peaks). For the neighboring EIT resonances, the velocities are several hundreds of meters per second, due to their large $\Delta\omega_p$. (It is seen in Fig. 2 that the spacings between

neighboring probe-laser resonances are several hundred MHz.) Since the rms velocity of the Maxwell velocity distribution in one dimension is about 170 m/s, the number of atoms contributing to the neighboring EIT resonances is greatly reduced relative to that of the center resonance. The finite width of the velocity distribution therefore limits the number of resonances observed in each scan to 2–4.

IV. DISCUSSION

According to Eq. (1), the paramagnetic shifts (which are all in the Paschen-Back regime) and the diamagnetism of the Rydberg atoms in strong B, lead to highly magnetic-field-sensitive shifts of the Rydberg-EIT resonances. For example, the cascade $|5S_{1/2}, m_j = -1/2\rangle \rightarrow |5P_{3/2}, m_j = -1/2\rangle \rightarrow |33S_{1/2}, m_j = 1/2\rangle$ generates an EIT peak that shifts at 7 MHz/G. The EIT resonances accessed in this work [boxed region in Fig. 4(a)] shift at about 2.5 MHz/G.

In Fig. 4, we show calculated B-field-induced Rydberg-EIT resonance shifts of both ^{85}Rb (thin red lines) and ^{87}Rb (bold blue lines). The shifts in Eq. (1) are highly dependent
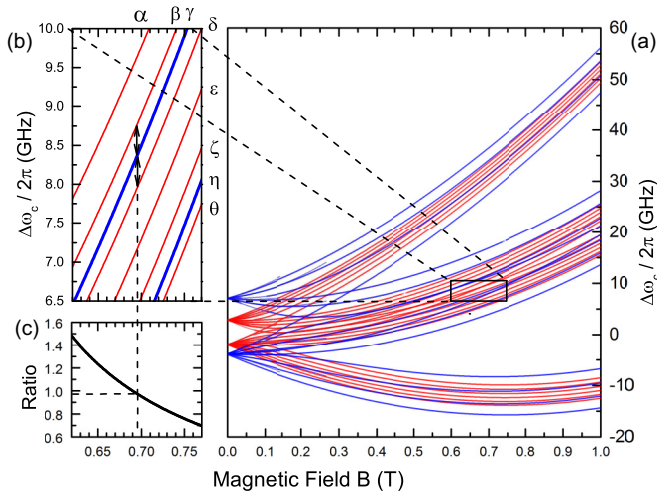
FIG. 4. (a) EIT line positions according to Eq. (1) as a function of B for π-π or π-σ transitions from $|5S_{1/2}\rangle$ through $|5P_{3/2}\rangle$ to $|33S_{1/2}\rangle$ for ^{85}Rb (thin red lines) and ^{87}Rb (bold blue lines). (b) Zoom-in of the transitions (α to θ) observed in this work. The arrows indicate the frequency separations $\Delta_{\beta\gamma}$ and $\Delta_{\gamma\delta}$ we use to extract the B field. (c) Splitting ratio $\Delta_{\beta\gamma}/\Delta_{\gamma\delta}$ vs B.
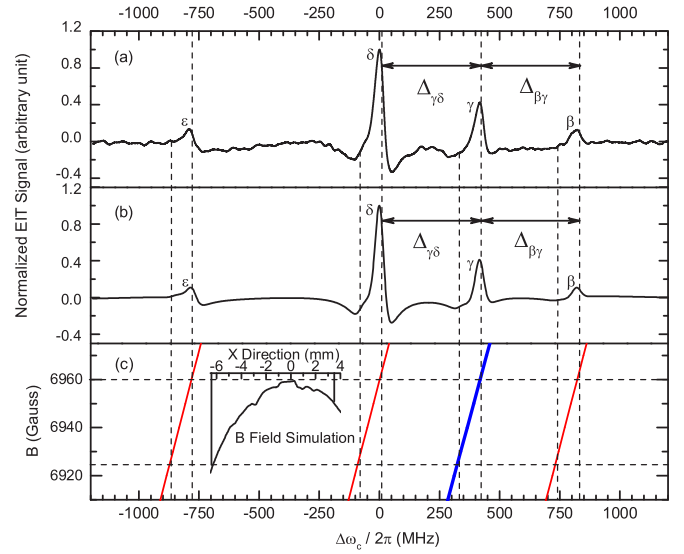

FIG. 5. (a) Zoom-in look of Fig. 3(d). (b) Monte Carlo simulation of the EIT spectrum shown in (a). (c) The magnetic field-induced EIT resonance shifts that contribute to the spectroscopic line-broadening and pulling for peaks ϵ, δ, γ, and β. The vertical dashed lines indicate the line-shape extent that results from the inhomogeneous magnetic field inside the cell. (Power broadening is on the order of 20 MHz). The inset shows the magnetic field, obtained from a FEM simulation, along the x-axis (cell boundaries indicated by vertical solid lines). The x-range is off centered by 1.5 mm to reflect possible asymmetry in the experimental setup.

on the B field, as shown in Figs. 3(g)–3(i). This leads to B-field-dependent differential shifts of the EIT lines of the two isotopes. This feature arises from the Paschen-Back behavior of $|5S_{1/2}\rangle$ and $|5P_{3/2}\rangle$. The arrows in Fig. 4(b) indicate the frequency splittings, the ratio of which we use to extract the B-field strength. We map the splitting ratio from the experimental data in Fig. 3(c) (horizontal arrows $\Delta_{\beta\gamma}/\Delta_{\gamma\delta} = 0.9685 \pm 0.0037$), using the function shown in Fig. 4(c), onto a magnetic field of $B = 0.6960 \pm 0.0008$ T (maximum field in the probe region). The quoted field uncertainty follows from the spectroscopic uncertainty of the peak centers of $\lesssim 1$ MHz (the probe laser linewidth) and standard error propagation in the mapping. Note the B fields derived from the Sat. Spec. and the EIT spectrum are slightly different because the respective laser beams pass through different regions of the B field [see Fig. 1(b)].

The spectra in Figs. 3 and 5 show that the EIT lines are asymmetric. This is in part due to the B-field inhomogeneity, which affects the line width (line-broadening), shifts the line centers (line-pulling), and causes the triangular shape of the EIT resonances. The origin of these effects needs to be reasonably well understood to confirm the accuracy of our B-field measurement.

In order to quantitatively model the spectra, we use a Monte Carlo simulation to find the power loss of the probe beam due to the photon scattering by the atoms in the inhomogeneous B field. The atoms are excited by laser beams with Gaussian profiles. The steady state of the excited-state population is calculated using the Lindblad equation for the three-level cascade structure [19] with position-dependent Rabi frequencies and magnetic-field-dependent level shifts. In the simulation, we randomly pick the atomic positions $\mathbf{R}_i = (X_i, Y_i, Z_i)$ from a uniform distribution truncated at the cell boundaries, and velocities in x direction from a one-dimensional Maxwell velocity distribution for 300 K (i is

the atom counting index). The B fields at positions $\mathbf{R}_i$ are given by the results of the FEM field calculation shown in Fig. 1 and in the inset of Fig. 5(c). The field-induced energy-level shifts are taken from data sets used in Figs. 3(g)–3(i). The probe and coupler Rabi frequencies, $\Omega_p(\mathbf{R}_i)$ and $\Omega_c(\mathbf{R}_i)$, are determined by the beam parameters given in Sec. II with center Rabi frequencies, $\Omega_{p0} = 2\pi \times 11$ MHz and $\Omega_{c0} = 2\pi \times 6.8$ MHz. Further, we consider the natural isotopic mix and assume a uniform distribution of the atoms over all m_i states. The probe detuning is set to $\Delta\omega_p = (\Delta E_e - \Delta E_g)/\hbar$ for the peak δ at $B = 0.6960$ T, the maximum B field along the beam path, and the coupler detuning is varied. The probe modulation (5 MHz peak to peak) is also taken into account. The spectrum is simulated using a sample of 10^6 randomly selected atoms. The averaged simulated spectrum is shown in Fig. 5(b).

The simulation agrees very well with the experimental spectrum, as shown in Figs. 5(a) and 5(b). Here, the B field inhomogeneity (see Fig. 1) dominates the line broadening. The B-field variation in the probe volume is about 3.5×10^{-3} T, which corresponds to a line broadening of ~ 100 MHz (vertical dashed lines in Fig. 5). The simulation also reveals that the line centers are pulled by the same amount of -10 MHz relative to the theoretical line positions expected for the maximum B field. Therefore, the ratio $\Delta_{\beta\gamma}/\Delta_{\gamma\delta}$ in Fig. 5(b), which we have used to determine the magnetic field in Fig. 4(c), is unaffected by the line pulling.

The only free parameter in the simulation is the decoherence rate of the Rydberg state. We have found that this parameter has a profound effect on the depth of the side dips next to all EIT peaks. In order to explain the experimentally observed

spectra, we have to assume a Rydberg dephasing rate of $2\pi \times 50$ MHz, with an uncertainty of ± 10 MHz. This dephasing rate is unexpectedly high, when compared to other Rydberg-EIT and Autler-Townes work [20,21]. This large dephasing rate might be due to free charges generated by Penning and thermal ionization of Rydberg atoms and magnetic trapping of the charges [22].

In the simulation we ignore optical pumping from the intermediate $|5P_{3/2}, m_j = 1/2\rangle$ into the ground level $|5S_{1/2}, m_j = -1/2\rangle$. We believe this is justified by the short atomfield interaction time (~ 200 ns), which allows only a few scattered photons per atom. We note that any optical pumping effects will only lead to a global attenuation of the EIT line strengths. Further, the EIT leads to a reduction in the probe-photon scattering rate, modifying the optical pumping near the EIT resonances [23]. In our case this is not expected to substantially alter the EIT line shapes. Optical-pumping could be, in principle, entirely avoided by selecting the $|5S_{1/2}, m_j = 1/2, m_i\rangle \rightarrow |5P_{3/2}, m_j = 3/2, m_i\rangle$ transition for the probe laser.

An important feature of Rydberg-EIT in strong B fields is the large diamagnetism of the Rydberg state, which enables the detection of small variations in a large magnetic field. Since the diamagnetic contribution to the differential dipole moment scales as $n^4 \times B$, the sensitivity of this measurement increases with B and it can be increased by going to higher n. In sufficiently high B fields and large enough n the Rydberg-atom spectrum becomes chaotic [24]. The Rydberg spectra in strong B field can be modeled to high precision ($\lesssim 10$ MHz uncertainty) [25]. In the fully chaotic regime, highly accurate calculations, covering energy regimes both below and above the field-free ionization limit, have been performed using large Sturmian basis sets and the complex coordinate method

[26]. The resultant added complexity of the spectra, combined with an ability to accurately model these spectra, will make Rydberg-EIT in high B even more sensitive to minute field variations.

V. CONCLUSION

We have studied vapor-cell Rydberg-EIT in a strong B field, in which ground, intermediate, and Rydberg states are all in the Paschen-Back regime. By exploiting the differential magnetic-field-induced shifts of the ^{85}Rb and ^{87}Rb EIT lines, we have measured $B = 0.6960$ T with a $\pm 0.12\%$ uncertainty. Simulated and observed spectra show excellent agreement. The spectra indicate an unusually large Rydberg-state dephasing rate, the origin of which is a subject for future work. Further, the large differential magnetic dipole moment of the diamagnetic Rydberg levels, which scales as B, suggests that the method holds promise for high-precision absolute and differential measurements of strong B fields. In Fig. 4, the maximum differential dipole moment at 0.7 T is $h \times 7$ MHz/G. Assuming improved experimental conditions (laser line widths < 100 kHz, a homogeneous magnetic field, and an uncertainty of 100 kHz of the EIT line center), for this line we expect a field-measurement uncertainty of 1.5×10^{-6} T. By extending the work to larger B fields and higher n, one may explore Rydberg-atom physics in the chaotic high-B regime in vapor-cell experiments.

[1] K. J. Boller, A. Imamoglu, and S. E. Harris, Phys. Rev. Lett. **66**, 2593 (1991).

[2] M. Fleischhauer, A. Imamoglu, and J. P. Marangos, Rev. Mod. Phys. **77**, 633 (2005).

[3] A. K. Mohapatra, T. R. Jackson, and C. S. Adams, Phys. Rev. Lett. **98**, 113003 (2007).

[4] V. Gavryusev, A. Signoles, M. Ferreira-Cao, G. Zürn, C. Hofmann, G. Günter, H. Schempp, M. Robert-De-Saint-Vincent, S. Whitlock, and M. Weidemüller, J. Phys. B: At. Mol. Opt. Phys. **49**, 164002 (2016).

[5] M. Tanasittikosol, J. D. Pritchard, D. Maxwell, A. Gauguet, K. J. Weatherill, R. M. Potvliege, and C. S. Adams, J. Phys. B: At. Mol. Opt. Phys. **44**, 184020 (2011).

[6] A. Tauschinsky, R. Newell, H. B. van Linden van den Heuvell, and R. J. C. Spreeuw, Phys. Rev. A **87**, 042522 (2013).

[7] M. Mack, F. Karlewski, H. Hattermann, S. Höckh, F. Jessen, D. Cano, and J. Fortágh, Phys. Rev. A **83**, 052515 (2011).

[8] J. Grimmel, M. Mack, F. Karlewski, F. Jessen, M. Reinschmidt, N. Sándor, and J. Fortágh, New J. Phys. **17**, 053005 (2015).

[9] M. Saffman, T. G. Walker, and K. Mølmer, Rev. Mod. Phys. **82**, 2313 (2010).

[10] J. Sedlacek, A. Schwettmann, H. Kübler, R. Löw, T. Pfau, and J. Shaffer, Nat. Phys. **8**, 819 (2012).

[11] C. Holloway, J. Gordon, S. Jefferts, A. Schwarzkopf, D. Anderson, S. Miller, N. Thaicharoen, and G. Raithel, IEEE Trans. Antennas Propag. **62**, 6169 (2014).

[12] D. A. Anderson, S. A. Miller, G. Raithel, J. A. Gordon, M. L. Butler, and C. L. Holloway, Phys. Rev. Appl. **5**, 034003 (2016).

[13] S. A. Miller, D. A. Anderson, and G. Raithel, New J. Phys. **18**, 053017 (2016).

[14] S. Bao, H. Zhang, J. Zhou, L. Zhang, J. Zhao, L. Xiao, and S. Jia, Phys. Rev. A **94**, 043822 (2016).

[15] D. J. Whiting, J. Keaveney, C. S. Adams, and I. G. Hughes, Phys. Rev. A **93**, 043854 (2016).

[16] D. J. Whiting, N. Sibalic, J. Keaveney, C. S. Adams, and I. G. Hughes, Phys. Rev. Lett. (to be published), arXiv:1612.05467.

[17] T. F. Gallagher, *Rydberg Atoms* (Cambridge University Press, Cambridge, 2005), Vol. 3.

[18] D. A. Steck, "Rubidium 85 D Line Data", available online at http://steck.us/alkalidata (revision 2.1.6, 20 September 2013) (unpublished).

[19] M. Tanasittikosol, C. Carr, C. S. Adams, and K. J. Weatherill, Phys. Rev. A **85**, 033830 (2012).

[20] B. J. DeSalvo, J. A. Aman, C. Gaul, T. Pohl, S. Yoshida, J. Burgdörfer, K. R. A. Hazzard, F. B. Dunning, and T. C. Killian, Phys. Rev. A **93**, 022709 (2016).

[21] H. Zhang, L. Zhang, L. Wang, S. Bao, J. Zhao, S. Jia, and G. Raithel, Phys. Rev. A **90**, 043849 (2014).

[22] E. Paradis, S. Zigo, K. Z. Hu, and G. Raithel, Phys. Rev. A **86**, 023416 (2012).

[23] L. Zhang, S. Bao, H. Zhang, G. Raithel, J. Zhao, L. Xiao, and S. Jia, arXiv:1702.04842.

[24] H. Friedrich, *Theoretical Atomic Physics* (Springer, Berlin, 2006), Vol. 3.

[25] E. Paradis, S. Zigo, and G. Raithel, Phys. Rev. A **87**, 012505 (2013).

[26] C. ho Iu, G. Welch, M. Kash, D. Kleppner, D. Delande, and J. Gay, Phys. Rev. Lett. **66**, 145 (1991).